LES STUDY OF THE IMPACT OF FUEL COMPOSITION ON A SWIRL SPRAY FLAME APPROACHING BLOW-OFF

A. Both[1], D. Mira[1] and O. Lehmkuhl[1]

[1] *Barcelona Supercomputing Center (BSC), Barcelona, Spain*

ambrus.both@bsc.es

Abstract

The present paper focuses on the large eddy simulation (LES) of the n-heptane and n-dodecane flames of the Cambridge swirl flames data repository (Sidey et al., 2017). The applied tabulated chemistry spray combustion model reproduces well the key phenomena controlling flame dynamics. The distinct volatility of the fuels is identified as the source of main difference between the n-heptane and n-dodecane flames.

1   Introduction

Spray combustion is the dominant fuel conversion method of the aerospace industry. The use of liquid fuels with high energy density is a common strategy to reduce the weight and increase the specific power in propulsion systems. However, the understanding of liquid fuel combustion requires fundamental concepts from multiphase flows besides the description of the combustion process. Advanced numerical techniques such as large eddy simulation (LES) (Pitsch, 2006) are becoming more essential in the development pipeline of aero-engines, as it gives insight into the highly transient phenomena that affects the range of operation and the levels of emission likewise.

This study is focused on the LES of a model aero-engine combustion chamber: the Cambridge swirl spray flame (Sidey et al., 2017). In particular, we concentrate on the differences between single component fuels like n-heptane and n-dodecane in order to obtain further understanding on the fuel effects on spray flames of aeronautical combustors.

This configuration has been the subject of various LES studies. Giusti and Mastorakos (2017) studied the strain induced localized extinction in a stable ethanol flame of this configuration using Conditional Moment Closure (CMC). Paulhiac et al. (2020) used a 2-step chemistry mechanism to study the flame structure of an n-heptane flame of this burner. Elasrag and Li (2018) studied n-heptane cases of the database using flamelet generated manifold based on premixed flamelets. Recently Foale et al. (2021) simulated a blow-off transient event using CMC to analyse the key phenomena leading to global extinction. In this study, the steady state behaviour of the system operated with different fuels is investigated using a tabulated chem-istry approach, which allows an important reduction in computational cost compared to other approaches based on the transport of species. This approach is similar to the work from Elasrag and Li (2018), but using stable and unsteady extinguishing counterflow diffusion flamelets.
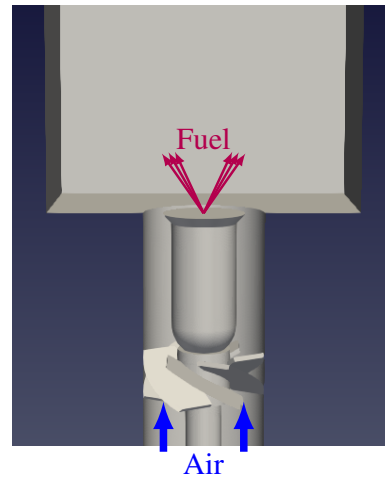

Figure 1: Illustration of the Cambridge swirl spray flame burner geometry.

Figure 1 shows the burner geometry. The domain is composed of an annular air inlet with a swirl generator, that surrounds the bluff-body that acts as a flame stabilizer. The plane of the bluff-body is aligned with an abrupt expansion of the cross section, as the air duct transitions into the combustion chamber. The bluff-body is cylindrically symmetric and reaches its highest diameter just before the entrance of the combustion chamber: $D = 25\,\mathrm{mm}$. The fuel injector is located in the center of the bluff-body, supplying fuel in a hollow cone pattern with a nominal spray angle of $60°$. The outer diameter of the air duct is $37\,\mathrm{mm}$. It joins in the center of combustion chamber, that has a square cross section of $95\,\mathrm{mm} \times 95\,\mathrm{mm}$ and length of $150\,\mathrm{mm}$. For further details on the burner geometry may be found in Yuan et al. (2018).

In all studied cases, the fuel is supplied at a rate of $0.27\,\mathrm{g/s}$. Both fuel and air are at ambient temperature, and the system is open to the atmosphere. The relevant cases of the Cambridge swirl spray flame database are summarized in Tab.1. Both H1S1 and DD1S2 are stable cases at the same gas phase Reynolds num-

ber, and very similar global equivalence ratio since the two fuels have comparable stoichiometric air fuel ratios: $AFR_{st,H} = 15.08$ and $AFR_{st,DD} = 14.92$ (in therms of mixture fraction: $Z_{st,H} = 0.0622$ and $Z_{st,DD} = 0.0628$). Note, that H1S1 and DD1S2 are the same in terms of air flow, but the two cases are significantly different, as the stable n-dodecane case is much closer to blow-off conditions than the n-heptane one.

	Fuel	U_b [m/s]	Re_g	ϕ_{glob}
H1S1	n-heptane	17.11	13500	0.32
H1B	n-heptane	22.8	18000	0.24
DD1S2	n-dodecane	17.11	13500	0.32
DD1B	n-dodecane	20.1	16000	0.27

Table 1: Global properties of the relevant cases of Cambridge swirl spray flame repository. H1S1 and DD1S2 are stable cases, while H1B and DD1B mark the onset of blow-off in the experiments. U_b: bulk air velocity at the entrance of the combustion chamber, Re_g: gas phase Reynolds number based on the bulk air velocity and the bluff-body diameter, ϕ_{glob}: global equivalence ratio.

In general terms, as a combined effect of the swirling air inlet, and the bluff-body geometry, a strong central recirculation zone (CRZ) is generated, that stabilizes the flame on the bluff-body. The flame takes an M shape, as it features inner and outer reaction layers. The inner reaction layer interacts with the spray and the recirculating reaction products, while the outer reaction layer is strongly disturbed by the high velocity swirling air and shows signs of shear induced extinction. Both layers show considerable intermittency. The presence of strong recirculation and localised extinction, and the significant droplet flame interaction pose a challenge to the numerical models.

In the rest of the present study, the modelling approach is briefly described including the gas and liquid phase models, then the numerical cases are introduced and compared with experiments. Finally, the behaviour of the different flames is studied, highlighting the effect of the fuel.

2 Simulation approach

The spray flame is simulated using our in-house finite element code Alya including a gas phase solver coupled with Lagrangian particle transport. These two components are described below .

Gas phase models

The Navier-Stokes equations are solved under the low Mach number assumption, i.e.: the gas density and the hydrodynamic pressure are decoupled, and the density is only a function of the thermo-chemical state. Consequently acoustic phenomena are neglected, relaxing the restrictions of time step size.

The momentum equation is solved with a non-

incremental fractional step method, while the thermo-chemical state is described with four transported scalars: enthalpy, mixture fraction, sub-grid mixture fraction variance, and progress variable. All equations are discretized in space using the same finite element grid. Linear finite elements are used resulting in a second order discretization in space, and the time marching is executed with a third order Runge-Kutta scheme (Both et al., 2020). The solved partial differential equations are presented below:

$$\partial_t \overline{\rho} + \nabla \cdot (\overline{\rho}\widetilde{\mathbf{u}}) = S_\rho^e, \tag{1}$$

$$\partial_t (\overline{\rho}\widetilde{\mathbf{u}}) + \nabla \cdot (\overline{\rho}\widetilde{\mathbf{u}} \otimes \widetilde{\mathbf{u}}) + \nabla \overline{p} - \nabla \cdot \tau(\widetilde{\mathbf{u}}) = S_{\mathbf{u}}^e, \tag{2}$$

$$\partial_t \left(\overline{\rho}\widetilde{h}\right) + \nabla \cdot \left(\overline{\rho}\widetilde{h}\widetilde{\mathbf{u}}\right) + \nabla \cdot \boldsymbol{\Phi}_h = S_h^e, \tag{3}$$

$$\partial_t \left(\overline{\rho}\widetilde{Z}\right) + \nabla \cdot \left(\overline{\rho}\widetilde{Z}\widetilde{\mathbf{u}}\right) + \nabla \cdot \boldsymbol{\Phi}_Z = S_Z^e, \tag{4}$$

$$\partial_t (\overline{\rho}Z_v) + \nabla \cdot (\overline{\rho}Z_v\widetilde{\mathbf{u}}) + \nabla \cdot \boldsymbol{\Phi}_{Z_v} = \tag{5}$$
$$-\overline{\rho}\chi_{Z_v}^{SGS} - 2\boldsymbol{\Phi}_Z^{SGS} \cdot \nabla \widetilde{Z} + S_{Z_v}^e,$$

$$\partial_t \left(\overline{\rho}\widetilde{Y_c}\right) + \nabla \cdot \left(\overline{\rho}\widetilde{Y_c}\widetilde{\mathbf{u}}\right) + \nabla \cdot \boldsymbol{\Phi}_{Y_c} = \tag{6}$$
$$\overline{\dot{\omega}_{Y_c}} + S_{Y_c}^e$$

where $\overline{\rho}, \widetilde{\mathbf{u}}, \widetilde{h}, \widetilde{Z}, \widetilde{Y_c}$ are the filtered density, velocity, enthalpy, mixture fraction, and progress variable, while Z_v denotes the sub-grid mixture fraction variance. Non-density weighted and Favre filtering are marked with bar and tilde superscripts using standard notation.

The total stress tensor is expressed as: $\tau = (\overline{\mu} + \mu_t) \left(\nabla\widetilde{\mathbf{u}} + \nabla^{\mathrm{T}}\widetilde{\mathbf{u}}\right) - \frac{2}{3}(\overline{\mu} + \mu_t) (\nabla \cdot \widetilde{\mathbf{u}}) \mathbf{I}$ considering the viscous and sub-grid diffusion of momentum. Here μ, μ_t, and $\mathbf{I}$ are the molecular viscosity, sub-grid viscosity, and the identity tensor respectively. The Vreman (2004) sub-grid model is used in this work.

The diffusive fluxes of enthalpy, mixture fraction, sub-grid mixture fraction variance, and progress variable are denoted by $\boldsymbol{\Phi}_h$, $\boldsymbol{\Phi}_Z$, $\boldsymbol{\Phi}_{Z_v}$, and $\boldsymbol{\Phi}_{Y_c}$ respectively. Each is composed of a molecular diffusion and a sub-grid scale transport component, for an scalar variable $\xi \in \{h, Z, Z_v, Y_c\}$ the fluxes are written as: $\boldsymbol{\Phi}_\xi = \boldsymbol{\Phi}_\xi^D + \boldsymbol{\Phi}_\xi^{SGS}$, where $\boldsymbol{\Phi}_\xi^D = -\overline{\rho}\widetilde{\mathcal{D}_\xi}\nabla\widetilde{\xi}$ is the flux of molecular diffusion, and $\boldsymbol{\Phi}_\xi^{SGS} = -\frac{\mu_t}{Sc_\xi}\nabla\widetilde{\xi}$ is the flux of sub-grid diffusion. The unity Lewis number assumption is followed for the diffusive scalar transport, thus the molecular diffusivity is: $\mathcal{D}_\xi = \frac{\lambda}{\rho c_p}$, whit the thermal conductivity λ and the specific heat c_p. Similarly all the gas phase sub-grid Schmidt numbers are taken equal: $Sc_\xi = 0.7$.

The sub-grid scalar dissipation rate of mixture fraction expresses the dissipation of its sub-grid variance, this term is modelled as: $\chi_{Z_v}^{SGS} = 2\frac{Z_v}{\tau_{SGS}}$ where

$\tau_{SGS} = \left(C_\epsilon^2 \frac{\mu_t}{\rho} \frac{|\mathbf{S}|^2}{\Delta^2} \right)^{-1/3}$ is the sub-grid time scale. Here $C_\epsilon = 3.24$ is a modelling constant of the sub-grid model, $\mathbf{S}$ is the strain rate tensor, and Δ is the grid size.

All equations are extended with a source term, that couples them to the Lagrangian particle cloud: S_ρ^e, $S_{\mathbf{u}}^e$, S_h^e, S_Z^e, $S_{Z_v}^e$, $S_{Y_c}^e$, for mass, momentum, enthalpy, mixture fraction, mixture fraction variance, and progress variable respectively.
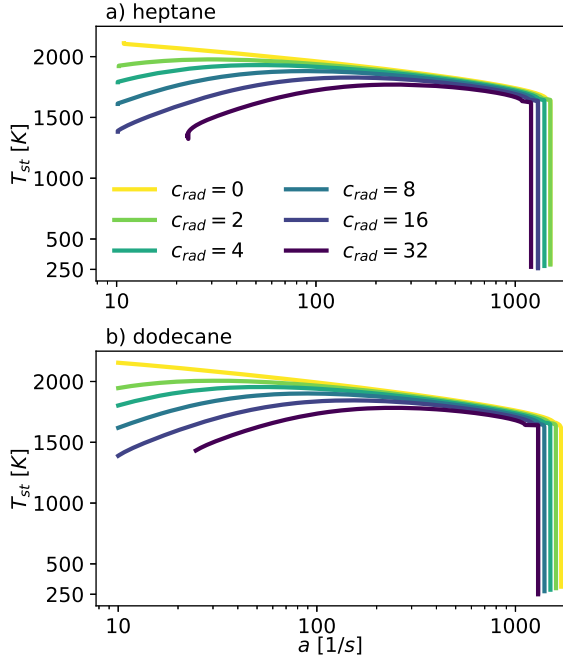
Figure 2: Temperature at the stoichiometric mixture in the flamelets included in the thermo-chemical database as a function of the applied strain rate. Different curves correspond to different scaling (c_{rad}) of the radiative term.

The thermo-chemical database is constructed from counterflow diffusion flames solved in physical space using Chem1D (Somers, 1994). N-heptane flamelets are computed using the mechanishm of Lu and Law (2006) containing 188 species and 939 reactions, while the mechanism of Kathrotia et al. (2018) is used for n-dodecane that includes 189 species and 1327 reactions. The databases are generated from steady solutions of the stable branch, and temporal samples of the unsteady extinguishing solution at a fixed strain rate, as illustrated in Fig.2.

In this work, two methods are applied simultaneously to account for enthalpy deficit: the inlet temperatures of the opposing diffusion flamelets are decreased, and a radiative heat loss term is included in the flamelet equations (Lammers and De Goey, 2004) multiplied with a scaling coefficient c_{rad} ranging from 0 (adiabatic) to 32.

Latter scaled radiative method has different effects along different points of the flame, since the higher temperature gasses suffer a higher heat loss. Furthermore, the strain rate of the opposing diffusion flame also affects the level of enthalpy deficit, as lower strains correspond to a higher residence time and thus allow higher amount of radiative heat loss.

The computed stable and unsteady extinguishing flamelets are represented by their stoichiometric temperatures and strain rates in Fig.2, for all 6 enthalpy levels of the two fuels. Steady flamelets are computed between $a_{min} = 10\ 1/\text{s}$ and the extinction point: a_{ext}, except for $c_{rad} = 32$ where no stable solutions are found below $a \approx 20\ 1/\text{s}$.

In terms of extinction and stoichiometric temperature, the two fuels are fairly similar. The maximum stoichiometric temperature of all flamelets only differs by less then 50 K: for n-heptane: $T_{st,H}^{max} = 2110$ K, and for n-dodecane: $T_{st,DD}^{max} = 2154$ K. The extinguishing strain rates are fairly close as well .The differences diminish with the transition to lower enthalpy levels, suggesting that the difference between the fuels is partially caused by the different fuel inlet temperature at the adiabatic level, that was taken as the boiling point of the fuels at atmospheric pressure.

The states along the flamelets are uniquely identified by the control variables: mixture fraction Z, progress variable Y_c, and enthalpy h. The mixture fraction is computed using Bilger's (1990) definition and the progress variable is computed as a liner combination of the species mass fractions. The progress variable definitions are optimized using a genetic algorithm (Both et al., 2021) that minimizes the occurrence of ambiguously identified flamelet states.

The progress variable is re-scaled, by the overall limits at each mixture fraction, thus the scaled progress variable is:

$$C = \frac{Y_c - Y_{c,min}(Z)}{Y_{c,max}(Z) - Y_{c,min}(Z)}. \qquad (7)$$

A similar normalization is applied for the enthalpy, with the difference that the scaling values are a function of both mixture fraction and progress variable. The normalized enthalpy is expressed as:

$$i = \frac{h - h_{min}(Z,C)}{h_{max}(Z,C) - h_{min}(Z,C)}. \qquad (8)$$

The counterflow diffusion flamelets are re-sampled along a rectilinear discretization of Z, C, and i to generate a table. Subsequently this table is PDF-integrated along the mixture fraction with a β-PDF as customary, to yield the full thermo-chemical database used in the LES calculations.

Spray models

Lagrangian particles are transported in the computational domain representing the spray cloud. Each particle is described by a set of ordinary differential equations (ODE) that describe the evolution of their location, velocity, mass, and temperature.

The motion of the droplets is tracked using a Newmark/Newton-Rhapson time integration scheme developed by Houzeaux et al. (2016). In this work the drag is determined by the Schiller-Naumann correction (1935).

The evaporation is modelled following Abramzon and Sirignano (1989), yielding ODEs describing the evolution of individual droplet temperature T_p and droplet mass m_p:

$$\frac{\mathrm{d}T_p}{\mathrm{d}t} = \frac{\pi d_p \lambda_{g,m} Nu_m^{*,AS}}{m_p c_{p,p}} \left(T_s - T_p\right) \frac{\ln\left(1 + B_T\right)}{B_T}$$

$$+ \frac{L_v}{m_p c_{p,p}} \frac{\mathrm{d}m_p}{\mathrm{d}t},$$ (9)

$$\frac{\mathrm{d}m_p}{\mathrm{d}t} = -\pi d_p \rho_{g,m} \mathcal{D}_{g,m} Sh_m^{*,AS} \ln\left(1 + B_M\right),$$ (10)

where d_p is the droplet diameter, $\lambda_{g,m}$ the mean gas thermal conductivity, $c_{p,p}$ the droplet specific heat, $Nu_m^{*,AS}$ the corrected Nusselt number, T_s the seen gas temperature, B_T the Spalding heat transfer number, and L_v the latent heat of evaporation. The terms in the mass transfer ODE are: $\rho_{g,m}$ the mean gas density, $\mathcal{D}_{g,m}$ the mean molecular diffusivity of the fuel vapour in the gas, $Sh_m^{*,AS}$ the corrected Sherwood number, and B_M the Spalding mass transfer number.

Equilibrium vapour mass fractions are enforced on the droplet surface. The gas properties are evaluated using the "1/3-law" (Yuen and Chen, 1976), while the liquid and phase change properties of the fuels are taken as a function of the droplet temperature following Daubert and Danner (1985). The Reynolds number dependence of the uncorrected Nusselt and Sherwood numbers are taken into account using the Ranz-Marshall correlation. (1952)

Configuration

Two computational grids composed by hybrid elements with refined boundary layers and tetrahedral elements in the bulk of the flow are tested are considered. A coarse grid characterized by a grid size of 1 mm in the region of interest yielding a mesh of 1.2M degrees of freedom, and a fine grid of 0.5 mm with 3.4M degrees of freedom.

The air inlet flow rate is prescribed upstream of the swirler as sown in Fig.1. The air inlet temperature is 288 K, while constant temperature boundary conditions of 700 K are imposed on the vertical and bottom walls of the rectangular combustion chamber to account for the wall heat loss. Note that the bluff-body is treated as adiabatic.

The computational droplets are introduced in the domain at the injection location with an initial temperature of 288 K. They are characterised by a truncated Rosin-Rammler distribution of $\overline{D} = 65\ \mu$m and width parameter $n = 2.5$. This size distribution is imposed for both fuels, the number of injected droplets in each time step is such, that the mean fuel mass flow rate is

recovered.

The initial droplet velocity is determined to recreate a hollow cone spray pattern. The droplets velocity direction is uniformly distributed azimuthally. The spray half angle is likewise selected randomly in a range cantered at $32°$ with a span of $\pm 8°$. The velocity magnitude is prescribed such, that the axial component of the initial velocity follows a normal distribution with an expected value of 18 m/s for n-heptane and 14 m/s for n-dodecane respectively, with a standard deviation of 10% in both cases.

3 Spray flame structure

The simulations of the H1S1 case were executed on the coarse and fine grid. The change in resolution has neglibile effect on the mean droplet cloud properties presented in Fig.3. Subsequently the DD1S2 flame was simulated using the coarse grid. Figure 3 shows good general agreement with the measurement results, the axial droplet velocity and Sauter mean diameter are reproduced well near the mean spray half angle, while disagreements are observed on the outer edge of the spray where the occurrence of droplets is lower.
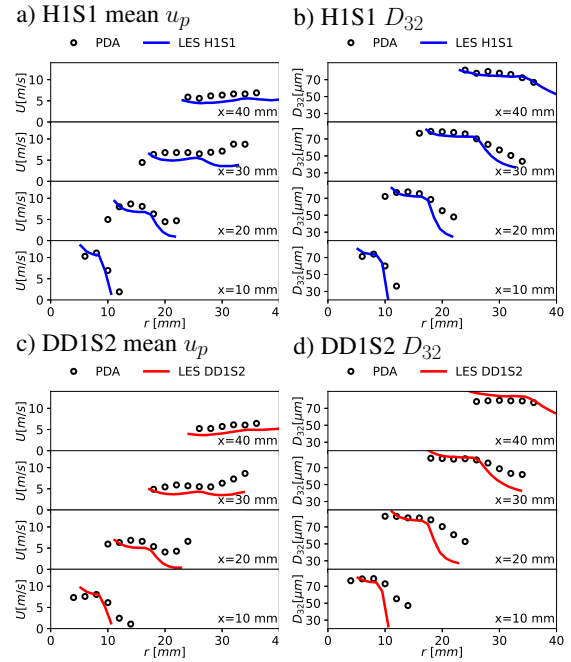

Figure 3: Comparison of mean droplet properties of the PDA measurements of Yuan et al. (2018) and the LES results of the present work.

The scaled control variables are shown on Fig. 4 illustrating which parts of the chemistry tables are accessed. The evaporation of the hollow cone spray creates a similarly hollow cone shaped mixture fraction field. This partially premixed mixture fraction structure ($\widetilde{Z} < 0.25$) can be clustered in three parts: 1) a low progress variable region is situated near the bluff-body ($\widetilde{C} \sim 0.4$) corresponding to the unsteady ex-

tinguishing flamelets in the thermo-chemical database; 2) a higher progress variable region enclosed between the inner and outer reacting layers ($\widetilde{C} > 0.7$); and 3) the flame surface itself that contains the transition from partially to fully reacted states. The scaled mix-
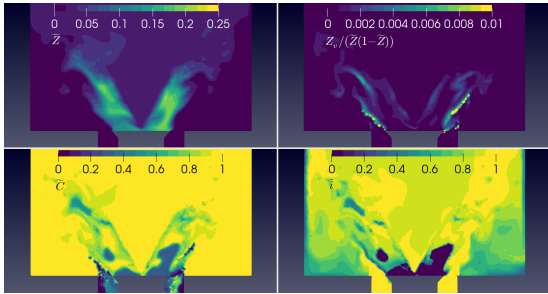
a) H1S1
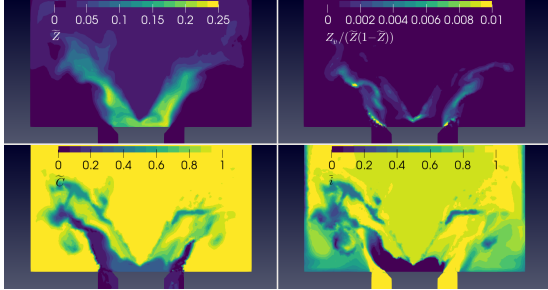
b) DD1S2

Figure 4: Instantaneous contours of the scaled control variables; top left: mixture fraction $\widetilde{Z}$, top right: scaled mixture fraction variance $Zv/(\widetilde{Z}(1-\widetilde{Z}))$, bottom left: scaled progress variable $\widetilde{C}$, bottom right: normalized enthalpy $\widetilde{i}$.

ture fraction variance is almost negligible, indicating that the modelling choices of the presumed-shape FDF model are of little importance. Finally the corner recirculation zones are characterized by medium normalized enthalpies ($\widetilde{i} \sim 0.5$) due to heat transfer to the burner walls, while the central recirculation zone is slightly below the adiabatic enthalpy level ($\widetilde{i} \sim 0.9$) mainly due to heat transfer between the gas and liquid phases. In other regions, the normalized enthalpy shows a high dependence on the scaled progress variable, as the scaling values depend on both mixture fraction and progress variable. In particular, the radiative heat loss method has more effect on low strains, thus the low progress variable regions (the flame surface and the region near the bluff-body) are characterised by lower normalized enthalpy.

Figure 5 and 6 show a cross section of the time averaged mixture fraction field and source term of mixture fraction from the droplet cloud. The mixture fraction highlights, that while the two fuels generate qualitatively similar structures, the lower volatility of n-dodecane results in significantly lower mixture fractions.

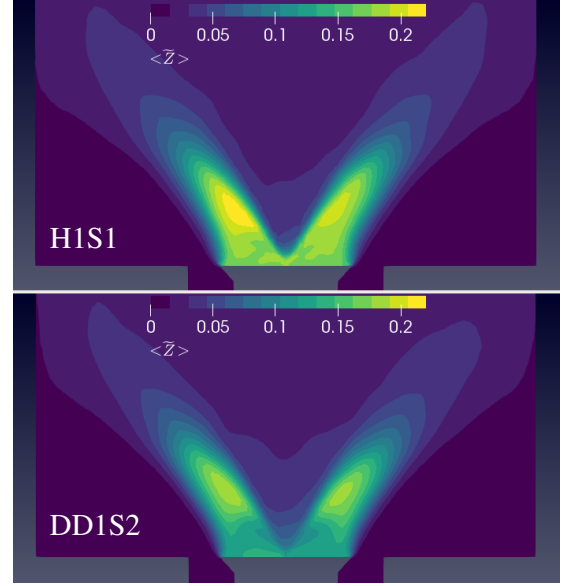The effect is highlighted by the average evapora-

tive source term. The main difference is in the magnitude of the source term peak. While in the n-heptane case the peak source term is over 60 kg/m^3s, in the case of n-dodecane it is less than half of this. The peak is located shortly after the injection, approximately in the same location in case of the two fuels.
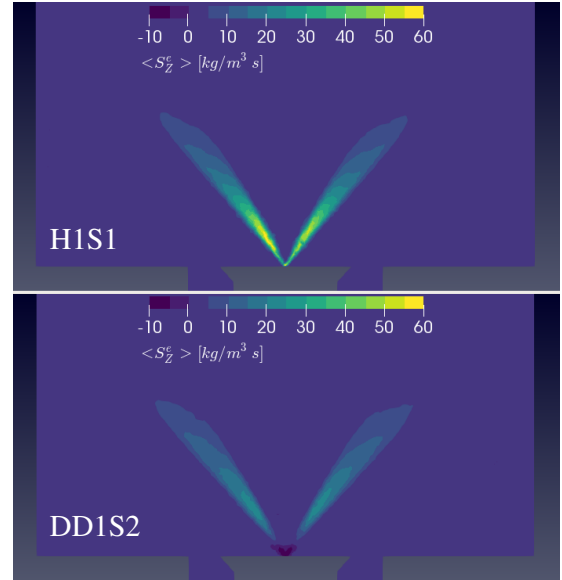

Figure 5: Temporal average of filtered mixture fraction.

Figure 6: Temporal average of mass source term generated by the evaporating droplet cloud.

The lowest iso-contour of $< S_Z^e >$ is more similar in the two cases. This suggests that the key difference between the two fuels is the time the droplets take to approach the saturation conditions that lead to high Spalding mass transfer numbers and high evaporation rates.

4 Conclusions

The H1S1 and DD1S2 cases of the Cambridge Swirl Flames Data Repository (Sidey et al., 2017) have been successfully simulated using LES. The applied spray model captures the mean droplet properties well, highlighting the importance of elaborate evaporation models in flames characterized by strong flame/droplet interaction. Our analysis suggests, that the main difference between the studied large hydrocarbon fuels originates from the different volatility of the two spray clouds.

Acknowledgments

References

Abramzon B. and Sirignano W.A. (1989) Droplet vaporization model for spray combustion calculations, *Int. J. of Heat and Mass Trans.*, Vol. 32, pp. 1605–1618

Bilger R.W., Stårner S.H. and Kee R.J., (1990) On reduced mechanisms for methane-air combustion in nonpremixed flames. *Combustion and Flame*, Vol. 80, pp. 135-149.

Both A., Lehmkuhl O., Mira D. and Ortega M. (2020) Low-dissipation finite element strategy for low Mach number reacting flows, *Computers & Fluids*, Vol. 200, pp. 104436.

Both A., Mira D. and Lehmkuhl O. (2021) Optimization of the progress variable definition using a genetic algorithm for the combustion of complex fuels, 10th *European Cobustion Meeting, Naples*

Daubert T.E. and Danner R.P. (1985) Data compilation tables of properties of pure compounds. Design Institute for Physical Property Data, American Institute of Chemical Engineers.

Elasrag H. and Li S. (2018) Investigation of Extinction and Reignition Events Using the Flamelet Generated Manifold Model. *Turbo Expo: Power for Land, Sea, and Air*, Vol. 51050, pp. V04AT04A023

Foale J.M., Giusti A. and Mastorakos E. (2021) Simulating the blowoff transient of a swirling, bluff body-stabilized kerosene spray flame using detailed chemistry, *AIAA Scitech 2021 Forum*, pp. 0187.

Giusti A. and Mastorakos E. (2017) Detailed chemistry LES/CMC simulation of a swirling ethanol spray flame approaching blow-off, *Proceedings of the Combustion Institute*, Vol. 36, pp. 2625-2632.

Houzeaux G., Garcia M., Cajas J.C., Artigues A., Olivares E., Labarta J. and Vázquez M. (2016) Dynamic load balance applied to particle transport in fluids *International Journal of Computational Fluid Dynamics*, Vol. 30, pp. 408-418.

Kathrotia T., Richter S., Naumann C., Slavinskaya N., Methling T., Braun-Unkhoff M. and Riedel U. (2018) Reaction Model Development for Synthetic Jet Fuels: Surrogate Fuels As a Flexible Tool to Predict Their Performance. *In Turbo Expo: Power for Land, Sea, and Air* Vol. 51043, pp. V003T03A008

Lammers F.A. and De Goey L.P.H. (2004) The influence of gas radiation on the temperature decrease above a burner with a flat porous inert surface, *Combustion and flame*, Vol. 136, pp. 533-547.

Lu T. and Law C.K. (2006) Linear time reduction of large kinetic mechanisms with directed relation graph: n-Heptane and iso-octane. *Combustion and flame*, Vol. 144, pp. 24-36.

Marshall W.R. and Ranz W.E., (1952) Evaporation From Drops—Part I. *Chem. Eng. Prog.*, Vol. 48, pp. 141-146.

Naumann Z. and Schiller L. (1935) A drag coefficient correlation, *Zeitschrift Verein Deutscher Ingenieure*, Vol. 77, pp. 318–323

Ottino G.M., Fancello A., Falcone M., Bastiaans R.J.M. and De Goey L.P.H., (2016) Combustion modeling including heat loss using flamelet generated manifolds: a validation study in OpenFOAM. *Flow, turbulence and combustion*, Vol. 96, pp. 773-800.

Paulhiac D., Cuenot B., Riber E., Esclapez L. and Richard S. (2020) Analysis of the spray flame structure in a lab-scale burner using Large Eddy Simulation and Discrete Particle Simulation, *Combustion and Flame*, Vol. 212, pp. 25-38.

Pitsch H. (2006) Large-eddy simulation of turbulent combustion. *Annu. Rev. Fluid Mech.*, Vol. 38, pp. 453-482.

Sidey J.A.M. , Giusti A., Benie P. and Mastorakos E. (2017) The Swirl Flames Data Repository, `http://swirl-flame.eng.cam.ac.uk`

Somers B. (1994) The simulation of flat flames with detailed and reduced chemical models (Doctoral dissertation)

Vreman A.W. (2004) An eddy-viscosity subgrid-scale model for turbulent shear flow: Algebraic theory and applications *Physics of fluids*, Vol. 16, pp. 3670-3681.

Yuan R., Kariuki J. and Mastorakos E. (2018) Measurements in swirling spray flames at blow-off, *International Journal of Spray and Combustion Dynamics*, Vol. 10, pp. 185-210.

Yuen M.C. and Chen L.W. (1976) On drag of evaporating liquid droplets *Combustion Science and Technology*, Vol. 14, pp. 147–154.